

Concentrating solar power (CSP) plant data-driven digital twin: a novel method for flux density prediction

Sergio Díaz-Alonso, Christian Raeder, Bernhard Hoffschmidt

German Aerospace Center (DLR), Institute of Solar Research, Im Langenbroich 13, 52428 Jülich, Germany

ARTICLE INFO

Keywords:

Concentrating solar power (CSP)
Digital twin
Cyber-Physical System (CPS)
Flux Density Measurements (FDM)
Real-time simulation

ABSTRACT

Concentrating solar power (CSP) is a promising renewable energy source because of its potential contribution to power generation and fuel synthesis (among others). However, several constraints continue to limit the economic and environmental attractiveness of this technology. One of the most important issues to address is measuring receiver efficiency, yet current methods are disruptive, expensive and complex. To overcome this, the present work introduces a data-driven digital-twin model for solar flux density predictions in central receiver systems (solar power towers). It consists of a real-time data agent that integrates signals collected at a CSP plant into flux density prediction tools. This flux prediction is coupled with a self-correction module based on graph neural networks (attention-gated U-Net) designed to replace simulations' mathematical with deep-learning algorithms trained on realistic flux density measurements. The outcome is a semi-autonomous cyber-physical model that achieves latencies below 30 seconds for common CSP operations and flux density characterization accuracies up to 95%, which makes it readily scalable, industrially applicable and more accurate than SOTA models. Its industrial relevance is boosted by a comprehensive training routine based on several heliostats' superposed fluxes at realistic conditions.

Nomenclature

Acronyms			
EU	European Union	DNI	Direct normal irradiation
CSP	Concentrating solar power	FDM	Flux density measurement
CST	Concentrating solar technologies	DT	Digital twin
LNG	Liquefied natural gas	CR	Central receiver
SPT	Solar power tower	CCD	Charged coupled device
PV	Photovoltaics	CMOS	Complementary metal-oxide-semiconductor
O&M	Operation and maintenance	CENER	Centro Nacional de Energías Renovables
NREL	National Renewable Energy Lab.	UTB	University of Texas at Brownville
GUI	Graphical user interface	DP	Data platform
BRDF	Bidirectional reflectance distribution function	GNN	Graphic neural net
Symbols			
F	Flux density measurement [MW/m ²]	$\dot{Q}_{pow,loss}$	Losses in the power block [MW]
\dot{Q}_{rec}	Power absorbed by the receiver [MW]	$\Delta\dot{H}_{HTF}$	Output heat in thermal fluid [MW]
$\dot{Q}_{rec,loss}$	Power loss in the receiver [MW]	η_{csp}	Performance of the CSP plant [-]
$\dot{Q}_{solar,in}$	Sun power [MW]	$\dot{Q}_{hel,loss}$	Heat loss in the heliostats [MW]
α	Elevation angle [°]	ϕ	Azimuth angle [°]
\vec{AP}	Aimpoint vector	\vec{n}_H	Active heliostat vector
E	Atmospheric extinction	\vec{TE}	Tracking error matrix
f_{int}	Interception factor [-]	A_H	Area of heliostat [m ²]
η_{rec}	Performance of the CSP plant [-]	η_{hf}	Performance of heliostat field [-]
ω_i	Sun incidence angle on heliostat "i" [rad]	A	Receiver area [m ²]

40

$$\dot{Q}_{solar,in} = \Delta\dot{H}_{HTF} + \dot{Q}_{hel,loss} + \dot{Q}_{rec,loss} + \dot{Q}_{pow,loss} \quad (3)$$

41

42 Afterwards, substituting eq. (3) in expression (2):

43

$$\eta_{csp} = \frac{\dot{Q}_{solar,in} - \dot{Q}_{hel,loss} - \dot{Q}_{rec,loss} - \dot{Q}_{pow,loss}}{\dot{Q}_{solar,in}} \quad (4)$$

$$\eta_{csp} = 1 - \frac{\dot{Q}_{hel,loss}}{\dot{Q}_{solar,in}} - \frac{\dot{Q}_{rec,loss}}{\dot{Q}_{solar,in}} - \frac{\dot{Q}_{pow,loss}}{\dot{Q}_{solar,in}} \quad (5)$$

44

45 The heliostat field (η_{hf}) and receiver (η_{rec}) power performances can be defined as:

$$\eta_{hf} = \frac{\dot{Q}_{hel}}{\dot{Q}_{solar,in}} = \frac{\dot{Q}_{solar,in} - \dot{Q}_{hel,loss}}{\dot{Q}_{solar,in}} \quad (6)$$

$$= 1 - \frac{\dot{Q}_{hel,loss}}{\dot{Q}_{solar,in}}$$

$$\eta_{rec} = \frac{\dot{Q}_{rec}}{\dot{Q}_{hel}} = 1 - \frac{\dot{Q}_{rec,loss}}{\dot{Q}_{hel}} \quad (7)$$

46

47 Another relevant non-dimensional scalar for flux correlations is the interception factor (f_{int}).
48 Sánchez-González and Santana [17] proposed the following correlation:

$$f_{int} = \frac{\bar{F} \cdot A}{DNI \cdot \sum_1^H \cos(\omega_i) \cdot A_{H,i}} \approx \eta_{rec} \quad (8)$$

49

50 The expression below can be then derived for CSP plant performance (eq. (5)):

$$\eta_{csp} = \eta_{hf} + \frac{\bar{F} \cdot A}{DNI \cdot \sum_1^H \cos(\omega_i) \cdot A_{H,i}} - \frac{\dot{Q}_{pow,loss}}{\dot{Q}_{solar,in}} - 1 \quad (9)*$$

51

52 In eq. (10), the authors demonstrate the explicit dependence between flux (F) and CSP performance.
53 Therefore, it is necessary to ensure a universal, cheap, virtual, continuous, accurate, and remote flux
54 density prediction to enhance CSP operation. The proposed approach addresses these challenges by
55 creating a digital twin (DT) that integrates real-time signals from the physical power plant and
56 incorporates a self-correction module based on deep-learning models trained with realistic and measured
57 data, what allows to shed mathematical models.

58 The main novel contributions of this work include: (i) a training routine based on superposed fluxes
59 (from several heliostats), (ii) subsequent superposed real-time flux inference, and (iii) the creation of a
60 data agent that interacts with the physical environment. The combination of this training routine with
61 the real-time monitoring increases the method's industrial relevance. The DT not only predicts
62 superposed fluxes but also tracks on-field variables (e.g. heliostat status) in real-time. This feature gives
63 the opportunity to track malfunctions or maintenance requirements while the DT operates. Owing to its
64 cyber-physical nature, the methodology is applicable to any of the existing CSP power plants and
65 summarized in [18], for tasks like aimpoint optimization [19-22], real-time monitoring or mere flux
66 prediction in specific timestamps.

67

68

69

70 2. State of the art: FDM and digital twins

71

72 2.1. FDM tools

73

74 The increasing flexibility requirements of CST have triggered the development of more complex
75 elements and operating conditions. Consequently, measurement techniques and devices - including flux
76 density measurement/prediction - must adapt accordingly. A summary of the current technical status is
77 provided below, inspired by ref. [15], and completed with later developments.

78

79 2.1.1. Direct methods

80

81 These methods rely on the use of sensors (radiometers or calorimeters) to monitor the measurand
82 itself in order to characterize the flux spatial distribution. Different configurations exist. First, stationary
83 sensor techniques consist of radiometer arrays positioned within the receiver domain randomly or in a
84 specified pattern. Accurate FDM is enabled in the precise spots where they are placed. However,
85 interpolation between these points is required to generate a continuous flux map. PS-10 plant has
86 employed this measurement procedure [23] and the expected lifetime of a constantly irradiated flux
87 gauge is only 6 months [24]. Second, sensors can be installed in moving bars or frames. In this case,
88 fast-response sensors are utilized, such as Gardon gauges or thin film heat flux sensors. Since the second
89 cited type can operate at up to 850°C, it is possible to avoid water-cooling circuits. Moreover, thin film
90 sensors' reduced size enables high resolutions, due to the possibility to densely stack a large number of
91 them. The sensor-equipped target is then translated across the receiver aperture plane. Linear bar systems
92 have shown accuracies around 94% with sufficient sensors and high-frequency acquisition devices [25].

93 Other techniques were designed in parallel to linear rods, like the rotating bar developed by eSolar,
94 designed to measure up to 5 MW/m² [26], or the moving alphanometer presented by Elsayed et al. [27].
95 However, these methods disrupt normal plant operation, and incur high maintenance and material costs.

96

97 2.1.2. Indirect methods

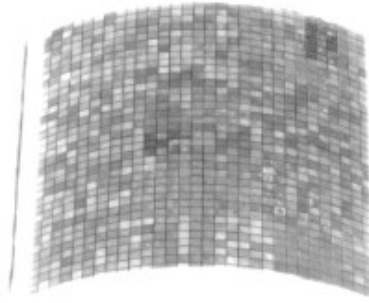
98

99 These procedures employ cameras to record the reflected radiation off the CR or Lambertian targets.
100 The resulting image is then scaled with a radiometer measurement in order to generate the flux map.
101 Several approaches are reported in the literature.

102 One option is to irradiate static or fixed Lambertian targets and capture the reflected radiation with
103 a camera. The result is a grayscale image, which has to be calibrated against a flux gauge. Calibration
104 consists of comparing the flux value provided by the radiometer with the gray value in its location. Then,
105 a complete flux map can be interpolated, considering the linear behavior and the gain factor of CCD or
106 CMOS sensors. Linear moving bars (analogous to the direct moving bars) represent the most widely
107 used alternative. Some examples of these technologies include HERMES [28] and HERMES II [24]
108 (with fixed targets) or PROHERMES [29] and FMAS [30] (with moving targets). Reported uncertainties
109 range from 3% (FMAS) to 40% (HERMES) can be expected. The maintenance of the moving parts and
110 the characterization of white target aging still hinder industrial application

111 On the other hand, open receivers enable the usage of the absorber surface as measurement target.
112 Finding the surface bidirectional reflectance distribution function (BRDF) is the first step, Offergeld et
113 al. [16] presented. After that, a picture of the receiver is taken, as depicted in the real *Solarturm Jülich*
114 (STJ) receiver picture from Fig. 2. The flux map can be generated considering the reflection properties
115 measured in the first scan and calibrating the gray values with a radiometer measurement. At the current
116 stage, uncertainties remain not acceptable for industrial usage (up to 40% [31]).

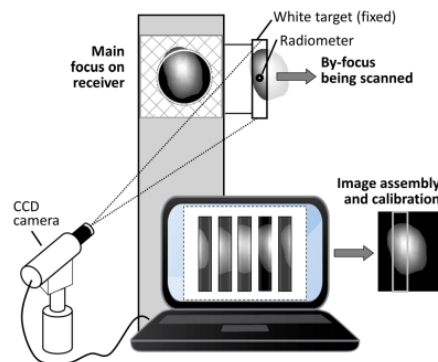
117



118
119

Fig. 2. Resulting image from a receiver scan.

120 Another indirect method uses a Lambertian stripe-shaped target and a moving focus. The calibration
121 of this method consists of moving a light beam across the stripe from left to right, as illustrated in Fig.
122 3. Several images are obtained during this displacement, and then, cropped and joined into a single
123 grayscale reconstruction of the light beam. This image is finally converted to flux scale in the same way
124 as in the rest of indirect methods. It was firstly mentioned in ref. [24], where uncertainties were found
125 to range from 20 to 40%.



126
127

Fig. 3. Schematic representation of the moving focus method [15].

128 These methods, often considered traditional FDM, present different limitations that the authors
129 address. Flux gauges remain the most accurate devices when their signals are properly conditioned.
130 However, their lifespan when they are directly irradiated and their costs (from 1500€ for Gardon gauges
131 to several thousand euros for Kendall radiometers) represent an obstacle in their application. Modern
132 rotating receivers also hinder their application due to the cabling complexity. In the case of indirect
133 methods, the systematic characterization of the irradiated surface, as well as the receiver coverage during
134 the flux measurement, limit their application in industrial environments. Furthermore, additional
135 structures cause expenses up to several thousand euros. Reported uncertainties here range from 3% to
136 40%, so most of the methods (except FMAS with a white target) are not applicable in industry. As a
137 result, the authors propose a cheap method, without physical infrastructure maintenance and primarily
138 software-based, what leverages the accuracy of recent simulation environments.

139

140 2.1.3. Computer based methods

141

142 Computing improvements have led to the deployment of more accurate, optimized, and fast ray-
143 tracing algorithms based on the Monte-Carlo method. Some examples are STRAL [32], Tonatiuh [33],
144 or SolTRACE [34].

145 Belhomme et al. [32] (2009) revealed STRAL's accuracy by comparing simulated flux maps and
146 indirectly obtained results for 4 single heliostats at CESA-1. The distance between the contour lines of
147 both methods was assessed. The RMSE between them ranged between 2.3 cm and 4.1 cm, what means
148 a deviation between 1.5% and 2.7% of the the light beam radius. Additionally, in ref. [15] (2014), the
149 simulated flux distribution presents mean deviations of -5% to 2%, standard deviations between 3.5%
150 and 4.5% and integrated power variations between -2% and 1% in the same radiation shield, compared

151 with state-of-the-art camera methods. However, input parameters have to be thoroughly studied and one
152 of the methods from 2.1.1 or 2.1.2 must be used to cross-check and validate the results, limiting ray-
153 tracer’s industrial application.

154

155 2.2. Digital twins

156

157 The term “digital twin” has been widely used since 2015, driven by the growth of data science,
158 computing capacity, AI, and communications. Rasheed et al. [35] defined a digital twin as “a virtual
159 representation of a physical asset enabled through data and simulators for real-time prediction,
160 monitoring, control, and optimization of the asset for improved decision-making throughout the life
161 cycle of the asset.”

162 Among the diverse current applications of DT, it is possible to find multiple energy-related “digital
163 twinning” examples in literature. In ref. [36], the authors present a coal plant digital twin, illustrating
164 the possibilities of cyber-physical systems for power plants. Other elements of renewable sources have
165 been virtually replicated, like steam turbines [37], windfarm cabling [38], or absorption chillers [39].

166 Nevertheless, DT examples in CST remain scarce. Machado et al. [40] employed Adaptive Neuro-
167 Fuzzy Inference Systems (ANFIS) and Partial Differential Equations (PDE) to model a Fresnel
168 collector, reaching 95% accuracy. M. Pargmann et al. utilized DT approaches enhanced with deep
169 learning for heliostat surface reconstruction and differentiable ray-tracing [41]-[42]. In these studies, the
170 authors outperformed the state-of-the-art ray-tracing simulations, by replicating heliostat surfaces
171 through the usage of data-driven models with inaccuracies below 0.7 mrad. Kuhl et al. [43] and Lewen
172 et al. [44] have reached accuracies between 84% and 92% in data-driven digital twins of heliostats used
173 for individual flux predictions.

174 However, those models still present some major constraints that the authors address in this work.
175 First, the flux prediction relies on the superposition of each heliostat’s light beam. As a consequence,
176 the deep-learning optimization can only be trained with individual flux maps under sunny conditions.
177 The low fluxes make these routines especially sensitive to meteorological conditions. Furthermore, the
178 training accuracy is dependent on the heliostat-target distance, and their computing costs make them
179 worthless for real-time superposed flux predictions. In addition, it is not possible to collect enough data
180 from every heliostat, what makes necessary to employ generalized (and not totally truthful) heliostat
181 surface data.

182 Even though Pargmann et al. outperformed SOTA simulations’ accuracies and Lewen et al. or Kuhl
183 et al. expanded those results, the present work aims to increase robustness and industrial suitability. In
184 this context, the authors aim to hybridize different techniques in order to combine the advantages of
185 each of them. The real-time data obtention from the physical environment ensures input’s accuracy; the
186 usage of STRAL leverages the proven accuracy of this software; and the introduction of deep-learning
187 corrections validate this method against experimental measurements while embedding physical-world
188 features to simulated superposed fluxes. The usage of superposed light beams reduces the training
189 sensitivity to meteorological conditions and allows further generalization in operation conditions.

190

191 3. Methodology

192

193 The aim of the presented methodology is to derive real-time superposed flux predictions on flat
194 surfaces with accuracies comparable to those of SOTA methods. The authors develop a connective and
195 quick data layer between the centralized data storage of Solar Tower Jülich (STJ) and a SOTA ray-
196 tracer. This approach represents a cost-competitive solution, since the only dedicated hardware
197 requirement is a commercial computer equipped with STRAL, an on-house ray-tracer. The rest of
198 hardware tools (heliostat controllers, sensors and storage systems) are required for the solar tower
199 operation, so the costs cannot be considered a flux-density-derived expense. Both the data agent and the
200 flux correction are open-source.

201 The digital-twin built upon the STJ centralized data platform (DP) [45] provides near real-time flux
202 predictions from meteorological and heliostat-related physically collected data. However, some

203 mathematical models (e.g. circumsolar ratio) are needed to complete the required ray-tracing
 204 simulations inputs. These assumptions can induce inaccuracies in the real-time DT flux maps that the
 205 authors address in this work by a self-correction based on convolutional neural networks (U-Net). For
 206 this task, the neural network is trained on grayscale images from camera methods, systematically
 207 comparing them with simulated flux maps. With the appropriate training routine, the neural network is
 208 able to predict the compound effect of all the modelled variables. A flow diagram of the complete
 209 procedure is provided in Fig. 4.

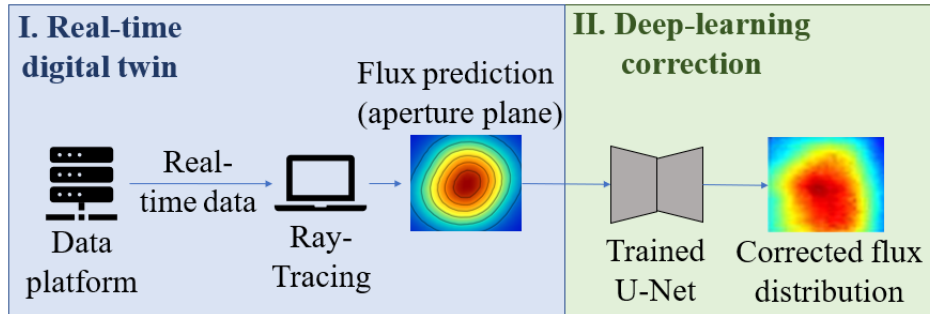


Fig. 4. Flow diagram of the self-corrected digital twin

210

211

212 3.1. Digital twin (DT) module

213

214 The first component of this flux prediction technique is the cyber-physical system (CPS), which
 215 clones in real-time the STJ within a virtual environment. It is composed of 4 interconnected layers, as
 216 depicted in Fig. 5: the physical world, the data storage layer, the computing engines, and the
 217 visualization module. The novelty of this module is the utilization of live data (collected from the plant)
 218 for simulation purposes in a ray-tracer engine. This data management is possible thanks to the 4.0 STJ
 219 data platform presented in [45], and the STRAL remote control from API.

220

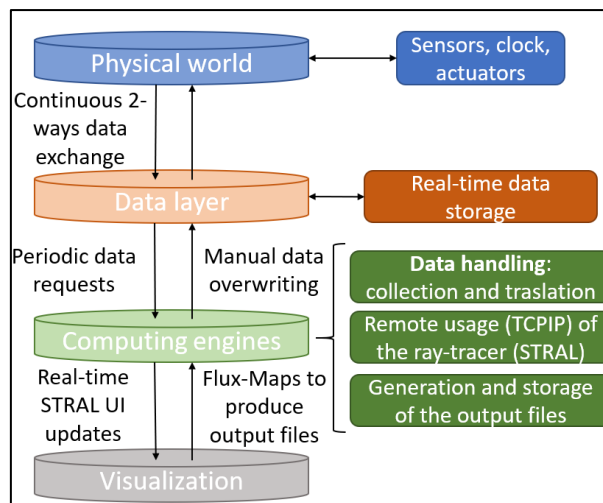


Fig. 5. Schematic representation of the different layers of the digital twin and their connections

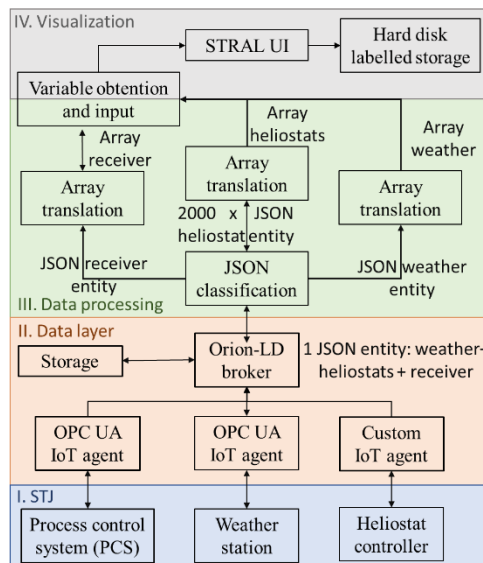
221

222

223 The first layer in this CPS, above depicted in blue, comprises the CSP plant and the different sensors
 224 that monitor both the operating and meteorological conditions. In this work, the prediction methodology
 225 is applied for *Solarturm Jülich* physical facilities. This research center is composed by two contiguous
 226 north-facing 60-metres high towers and 2000 heliostats of 8 m². Weather and operating conditions are
 227 monitored in real time by different sensors scattered across the CSP plant. A meteorological station
 228 equipped with a pyrliometer, an anemometer, a thermometer and a barometer collect the
 229 meteorological conditions. Likewise, information about each heliostat's actuators, tracking status and
 230 aimpoints is clustered. Finally, heliostats' reflectivities are manually measured and logged before
 231 experiments.

232 Miadowicz et al. [45] identified the potential benefits of centralizing the storage of this physical
 233 data, initially backed-up on separate offline devices. In response, they created the “data layer” from Fig.
 234 5, which combines open-source and self-built services to integrate the legacy sensors and storage
 235 systems previously mentioned. FIWARE was selected by the authors as the open-source IoT platform
 236 to implement the whole data model. Its flexible generic enablers provided wrappers for the integration
 237 of the legacy OPC DA data loggers, a normalized data structure (NGSI-LD), and a data broker for
 238 external access (Orion-LD). Real-time storage is deployed on a Kubernetes-based system, connected to
 239 the broker by MongoDB, a popular open-source tool for live database management.

240 The availability of these live and comprehensive data flows motivated the authors to enhance Monte
 241 Carlo ray-tracing performance. As mentioned in 2.1.3, the leverage of live physical data reduces the
 242 dependency of ray-tracing results on inputs quality. To this end, this work presents an open-source agent
 243 to translate in near real-time all the data from the standard DP and to feed it directly into a simulation
 244 environment. The agent queries the Orion-LD broker, where all the information is contextualized, and
 245 receives a data package containing the virtual entities and metadata provided by the context server. As
 246 all database modules are standardised, the queried data package is received by the agent in standard
 247 JSON format. The agent first unpacks the information into the different entities, then translates the
 248 standardized JSON bodies into non-standardised STRAL-compatible arrays. Finally, the translated data
 249 is fed into the ray-tracer remote functions, so it can be controlled from the data API too. An SSH tunnel
 250 between the client and the DP, and a TCP-IP link between the client and the ray-tracer remain open for
 251 the correct data exchange, summarized in Fig. 6. The SSH link and the DP information are protected by
 252 a standard OAuth2-based identity verifier, which the presented agent must satisfy during deployment.



253 **Fig. 6.** Complete data itinerance from sensors to stored flux maps (same colour code as in Fig. 5).

254

255 Although the DT lacks a dedicated GUI at this stage, the ray-tracer front-end is employed to display
 256 all the information (grey block above). The operating heliostats, their aimpoints, the receiver location,
 257 the towers’ shading and all the meteorological conditions are represented. This virtual environment
 258 incorporates the real heliostat surfaces obtained from the last deflectometric campaign. Furthermore, the
 259 tracking errors are periodically updated in this model using camera-target calibrations. During
 260 simulations, the flux maps are automatically labelled with date and time and stored on the hard disk.
 261 Thus, it is also possible to monitor flux while the ray-tracer works synchronously and displays the field
 262 information.

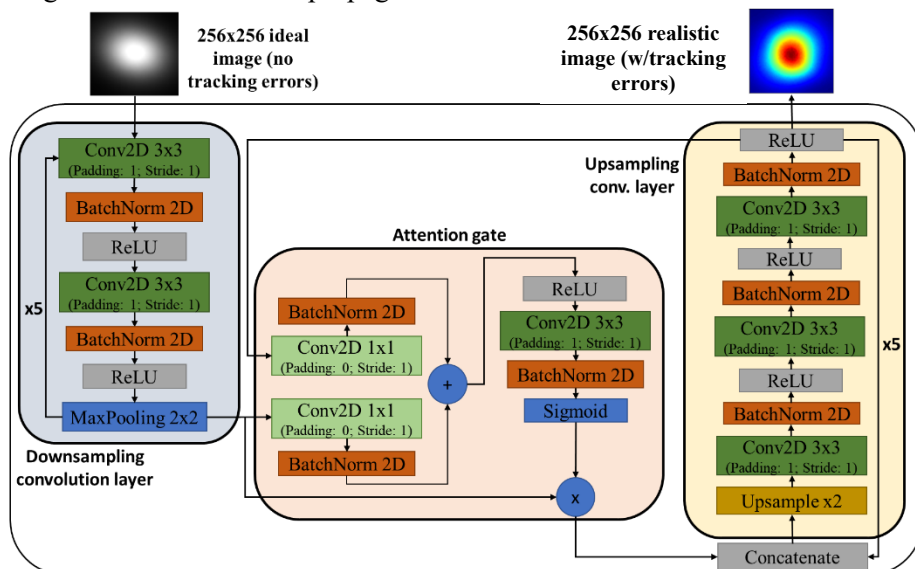
263 The DT automatically updates several parameters in real-time too, such as each of the heliostats’
 264 aimpoints (including stow and defocus positions); their slope errors - if camera-target procedure is
 265 performed; heliostat actuators malfunctions; their average reflectivity; and the flux evaluation plane
 266 position, orientation and size. Additionally, DNI and sun positions are updated continuously thanks to
 267 the weather station.

271 The second component hereby presented is a deep-learning model capable of correcting inaccuracies
 272 in DT outputs caused by input mathematical models (e.g. atmospheric extinction). The use of direct or
 273 indirect methods allows to characterize these effects employing physical measurements. Thus, the
 274 authors have chosen AI methods to provide the model with indirect FDM methods' information. In
 275 particular, graphic neural networks (GNN) are being tested to systematically compare simulated flux
 276 maps with physically measured ones.

277 As discussed in the state-of-the-art, the drawbacks of these accurate and proven camera-based
 278 measurement methods are high costs, complexity and operation disruptions. Therefore, the authors
 279 pretend to eliminate mathematical models' impact on DT performance by using information from them,
 280 and subsequently, dismantle the camera system for daily operation. With this aim, a dataset of indirectly
 281 measured flux maps in the aperture plane of the receiver is collected alongside equivalent fluxes
 282 simulated with the DT approach. After this measurement campaign, the neural network can be trained
 283 by systematically comparing both input sources (simulations and physical measurements).

284 The neural network used in early development is a tuned U-Net [46], based on U-shaped encoder-
 285 decoder structures with serial convolutional filters. This architecture is adapted to the specific task of
 286 flux profiles mapping. First, the input and output dimensions are defined as $1 \times 256 \times 256$, what
 287 corresponds to grayscale (1-channel) images of 256×256 px. The encoder layers sequentially compress
 288 5 times the input into a latent representation, enabling the network to extract the essential features at
 289 different resolutions. Then, the decoder layers upsample 5 times to restore the original dimensions while
 290 preserving the input integrity.

291 This modified neural network has been also equipped with multi-class attention gates, first proposed
 292 by Liu et al. [47], as displayed in Fig. 7. These gates enhance the topographical information perceived
 293 by U-Net along each isoline band. Finally, the original binary cross-entropy loss function is replaced by
 294 pixel-wise mean-square error loss (MSE or L2-loss). This transformation is essential for reproducing
 295 continuous distributions instead of binary masks. While binary cross entropy loss function assesses the
 296 differences in case of binary masks, as it only computes 0 and 1 values, L2 loss computes continuous
 297 values in order to inform the neural network about the current prediction ability. Since the dataset
 298 comprises images with normalized continuous values between 0 and 1, a BCE loss would not provide
 299 useful learning information for backpropagation.



300 **Fig. 7.** Multi-layer attention-gated U-Net. This block represents each of the 5 layers from this neural network.
 301 Input channels per layer are [1,64, 128, 256, 512, 1024].

302 This U-Net has been trained by systematically comparing pairs of images with the same resolution
 303 and number of channels, using the dataset developed at 4.2.. The images are cropped to 1440×1440 px

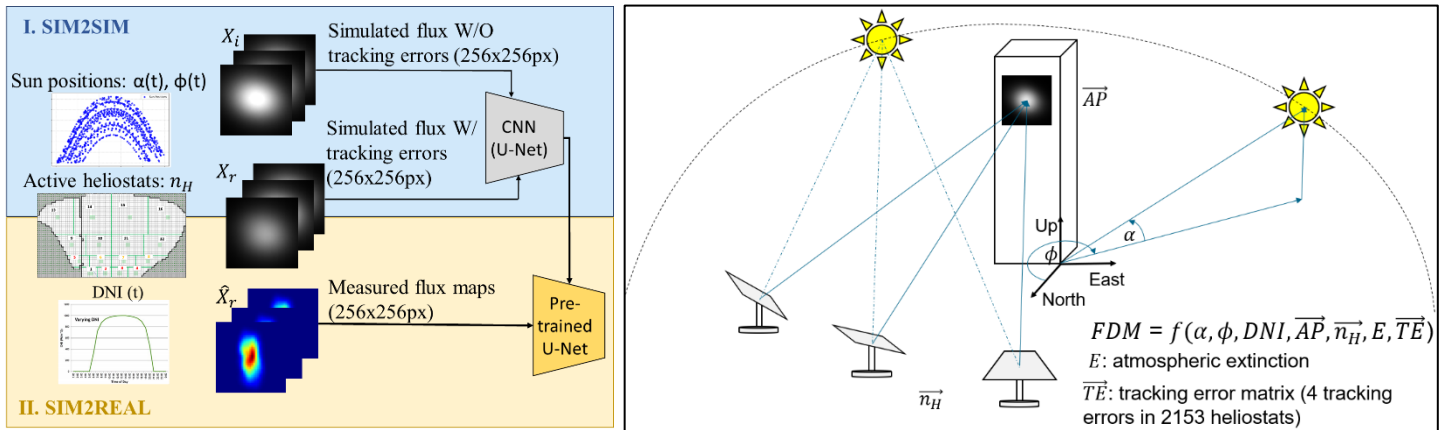
304 and downsampled to 256x256px to reduce computing time, while preserving the most important
 305 features. As mentioned in 4.2, each pair of images is composed of a flux map derived from simulations
 306 without and with tracking errors, respectively. Considering the synthetic nature of the pre-training
 307 dataset, the authors added random noise maps with a PSNR of 2.5% to 20% of the images, as well as a
 308 180° vertical or horizontal flip of another random 20% of the images, in order to augment the dataset.
 309 With these inputs, the neural network is capable of learning the relations between input and ground-
 310 truth features, and later infer an output with the ground-truth features, given an input. As seen in Fig. 4,
 311 the flux prediction from the DT is used as the input of the trained neural network. This NN was
 312 previously trained by comparing predictions with camera's measurements.

313 The main parameters defining the results of flux predictions/measurements are the sun position
 314 (azimuth and elevation angles, ϕ and α), DNI, aimpoints (\overline{AP}), number and location of active heliostats
 315 ($\overline{n_H}$), atmospheric extinction (E) and tracking errors (\overline{TE}), as introduced in eq. (10).

$$316 \quad 317 \quad 318 \quad FDM = f(\alpha, \phi, DNI, \overline{AP}, \overline{n_H}, E, \overline{TE}) \quad (10)$$

319 A correct training process needs to present enough variability in each of these governing parameters
 320 and a soft learning process. This ensures that the NN will be able to learn all the different combinations
 321 from given flux maps. Considering the dimensional complexity of this problem, the authors have divided
 322 the U-Net training in two steps: sim2sim and sim2real, depicted in Fig. 8, left. The first stage (sim2sim)
 323 is considered a pre-training, based on the comparison between grayscale flux maps obtained from
 324 simulations with tracking error models (X_r) and without them (X_i). The aim in this step is to teach the
 325 neural network the effect of sun position, DNI and number of heliostats (check Fig. 8, right), leaving
 326 atmospheric extinction and aimpoints as constant parameters. The ray-tracer information about the
 327 mentioned training parameters is sufficiently precise to consider it a real learning for the final inference
 328 with camera methods. Furthermore, the tracking error models' effects are used to quantify the mapping
 329 ability of this NN. If this training is successful, the neural network will then be able to estimate the effect
 330 of the tracking error models, given a simulation without tracking errors (X_i).

331 **Fig. 8.** U-Net complete training routine (left) and sim2sim step conceptual map (right).



332 In the second step of the training process, the pre-trained model will be used to learn the relations
 333 between predictions with tracking errors (X_r) and real measurements (\hat{X}_r). This process will provide the
 334 model with real information about atmospheric extinction and real tracking errors.

335 In 4.3, the authors show the successful results of the sim2sim training step, using 4.2 training dataset.
 336 The result is a simulated superposed real-time flux in flat surfaces that predicts the effect of tracking
 337 error models.

338

339

340 4. Results

341

342 This work evaluates the capabilities of a novel self-corrected digital-twin-based flux prediction
 343 approach. The first key performance metric here analyzed is prediction latency, using common reference
 344 instructions at STJ during daily operation to evaluate the data agent’s pre-processing ability (section
 345 4.1). Then, the automatic generation of a complete dataset for AI-training is demonstrated to evaluate
 346 the performance of post-processing and its industrial applicability. Finally, sim2sim correction results
 347 are presented, emphasizing the main purpose of this self-corrected DT: accurate live flux predictions. In
 348 this case, the key performance metrics are: peak and average deviations between flux predictions and
 349 their ground-truths, the inference MSE loss, and an image-replication accuracy function defined in 4.3.
 350 Their statistical significances are evaluated by using 95% confidence intervals (CI) across the 63
 351 samples studied.

352

353 *4.1. Proof of concept: latency analysis*

354

355 The term “latency” here refers to the time between the data package obtention from the DP and the
 356 generation of the RGB flux map. According to [45], the latency within the data platform is around 100
 357 ms that should be added to the results hereby presented. The authors aim to find the relation between
 358 the size and complexity of digital twin instructions and the model’s response time. For this analysis, the
 359 power plant constant parameters are defined as shown in Table 1 and remain unmodified during the
 360 whole latency assessment.

361

Table 1. Constant parameters for STJ + MFT replica

Static parameters	STJ+MFT
Plant location (deg.)	(50.913,6.388)
Plant height (m)	110
CSR (%)	5
Heliostat number	2153
Dimension of hel. (m ²)	8
Facets	4
Initial reflectivity	0.92 (clean, new)
Receiver height (m)	35 (centered in MFT)
Tilt angle of receiver (deg)	15
Evaluation plane size (m ²)	4 x 5.5
Atmospheric extinction	Leary-Hankins model

373

374 With these parameters loaded into the model, the digital twin was tested. It was then operated to
 375 iteratively access the data , i.e. to monitor in real-time. The authors aimed to replicate typical daily
 376 operations in a CST plant with varied instruction sizes, as summarized in the left column from Table 2.
 377 Each of the instructions was executed independently in order to meticulously control the cause of
 378 latency. The latency results below are the averaged times of 10 repetitions per instruction.

379

380

Table 2. Latency results in automatic mode (STJ).

Operation	Latency (s)
New sun position, time and DNI	4.86
5, 50, 500 heliostats defocused	7.4; 11.1; 24.2
New aimpoint definition	3.42
Change of aimpoint (5,50, 500)	8.2; 12.3; 26.8
Change of tracking error (5, 50, 500)	9.6; 18.1; 29.2
New average reflectivity	4.79

388

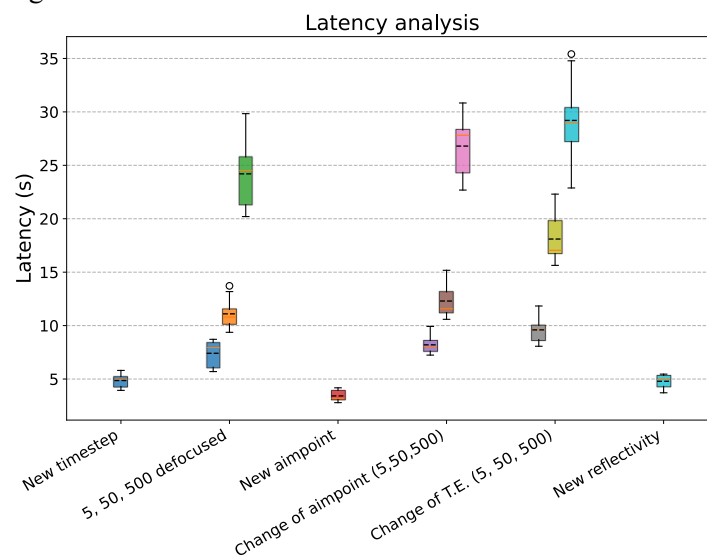
389 In order to elucidate the latency trends and how they can be improved, it is required to understand
 390 the amount of data entities involved in each instruction. The first instruction requires the update of a
 391 single data entity: “Weather”. This entity contains 8 variables, but only 5 are updated with this operation:
 392 azimuth, elevation, DNI, date and time. This update occurs every time the DT is executed, so its latency

393 is especially important. Both the third and sixth instructions imply the update of a single entity:
 394 “Receiver” and “Heliostat field”, respectively. Defining a new aimpoint requires the modification of
 395 three variables (X, Y and Z aimpoint’s position), and updating the reflectivity requires only one
 396 parameter. However, modifying this value also requires the download and traslation of the “Heliostat
 397 field” entity, which is directly linked to the 2153 “Heliostat” entities. This resource-consuming data
 398 itnerance explains why this operation takes a 33% more time than the aimpoint definition.

399 Heliostat defocusing requires a “get” query for each of the defocused entities. Furthermore, the three
 400 components of the heliostat aimpoint are varied. Thus, defocusing heliostats involves three times more
 401 parameters than the number of modified mirrors. The same number of parameters is involved in the
 402 change of aimpoint for a set of heliostats, which explains the similar processing times for both
 403 instructions. It is possible to appreciate in both cases that increasing ten times the number of involved
 404 heliostats approximately doubles the processing times. However, it is plausible to elucidate that the
 405 percentage variation will get exponentially bigger when 10 times more heliostats are defocused for
 406 bigger fields (5000, 50000....). This conclusion lies in the fact that the variation from 5 to 50 heliostats
 407 is a 50% for both second and fourth instructions, but a 118% and 117% from 50 to 500 heliostats.

408 Finally, the update of tracking error values is analyzed. 5, 50 and 500 heliostat entities are again
 409 involved in this complex update, but now 4 parameters are required to characterize each tracking error.
 410 This difference increases a 33% the number of updated parameters, what has a direct impact in the
 411 processing time. Compared to the previous instructions, the processing time increases between a 15%
 412 and 50% for this case.

413 In order to have a better understanding of these results, the complete latency analysis is provided as
 414 a family of boxplot diagrams below.

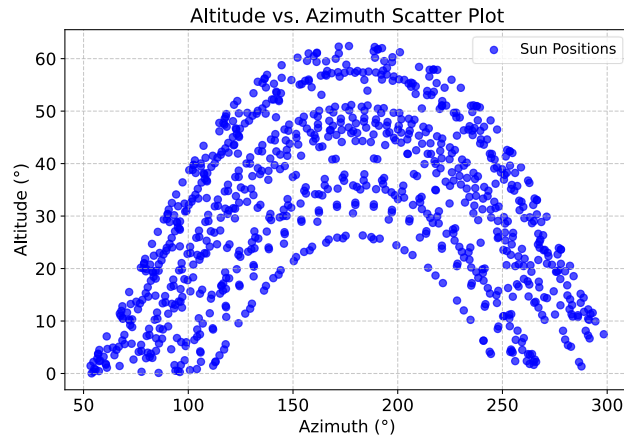


415 **Fig. 9.** Latency analysis' boxplot. 10 samples per value.

416 **4.2. Dataset generation for AI-enhancement**
 417

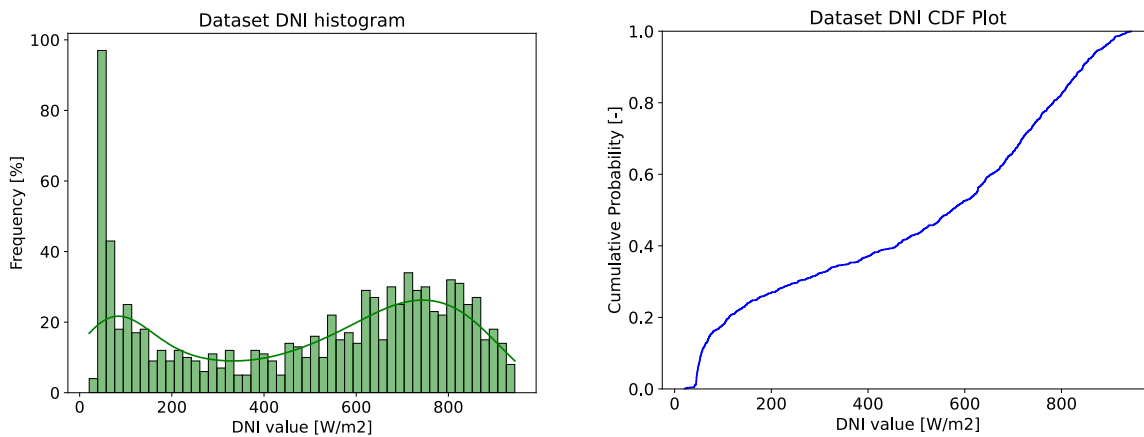
418 The DT algorithm has been used for the automatic and quick generation of the pre-training dataset.
 419 It is composed of 15827 pairs of 1920x1440 px grayscale simulated flux maps from the aperture plane
 420 of the second level of the MFT (35 metres high and 15° tilted). Considering that aimpoint combinations
 421 and atmospheric extinction are not training parameters during sim2sim step, they remain constant for
 422 all simulated cases. The aimpoint used for the whole dataset is located at the geometric center of the
 423 mentioned receiver. The simulations replicate 931 realistic environmental conditions from DLR
 424 experiments between March, 2014 and September, 2016.

425 First, the dataset must provide intrinsic information about the flux maps' features related to each
 426 meteorological factor. Therefore, the different selected conditions are thought to sufficiently represent
 427 every sun trajectory, i.e. every pair of azimuth and elevation values to be later inferred. The filtered solar
 428 data is depicted in Fig. 10. This dataset provides enough information about the azimuth values between
 429 50° and 300° and the altitude/elevation values between 0° and 62°, which are the representative intervals
 430 for the STJ latitude.



431 **Fig. 10.** Dataset's azimuth-altitude graph

432 For this dataset's aim, it is also required to sufficiently represent all meaningful DNI values. After
 433 gathering the DLR archive and usual operating conditions, DNI values between 50 W/m² and 942 W/m²
 434 have been recorded in Jülich. The histogram (left) and cumulative distribution function (CDF, right) are
 435 shown in Fig. 11. The histogram shows a higher representation of limit values (both high and low DNI),
 436 because the U-Net is able to infer the intermediate values. In fact, the DNI is lower than 200 W/m² in a
 437 27% of the reproduced conditions and higher than 600 W/m² in a 47%. Since this dataset will be used
 438 to train a neural network capable of predicting flux distributions for DNIs between 50 W/m² and 942
 439 W/m², 74% of the training conditions teach the neural network only 55% of the DNI values.
 440 Furthermore, DNI values below 100 W/m² are proportionally even more represented than the rest. The

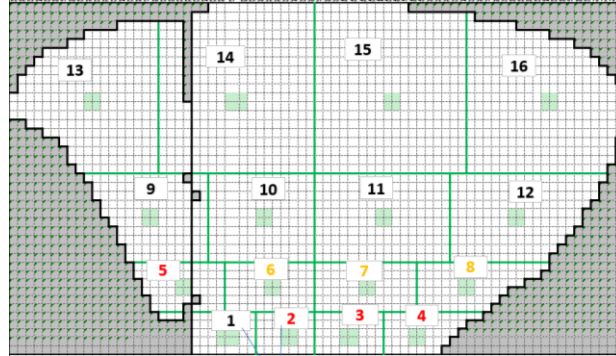


441 reason is the fewer features that a low flux image (potentially caused by low DNI) carries. Grayscale
 442 values in such cases range from 0 to 50, whereas in high-flux images, they range from 0 to 230. This
 443 variety of DNI values comprises clear conditions (750-942 W/m²); hazy conditions with diffusive high
 444 clouds (450-750 W/m²) and low clouds intervals.

445 **Fig. 11.** Histogram (left) and CDF (right) of the DNI values comprehended in the dataset

446 The last parameter to be studied is the number of active heliostats. In this concern, each of the 16
 447 areas depicted in Fig. 12 were individually defocused and the 931 conditions were simulated. In other
 448 words, the whole heliostat field is simulated for the 931 meteorological conditions; then area 16 is

449 defocused and the process repeated; afterwards area 16 is refocused, the area 15 is defocused, and the
 450 conditions are again tested, etc. The constant parameters of the simulation remain unchanged from the
 451 previous section. Due to the industrial scope of this approach, heliostats' combinations with more than
 452 one defocused area were not tested. It can be considered that most heliostats operate under usual
 453 industrial regimes, and hence, the U-Net does not need to learn those cases in which few mirrors are
 454 focused.



455
 456 **Fig. 12.** Schematic of the dataset's 16 stochastic heliostat areas

457 This dataset ensures enough variability to cover a wide spectrum of flux maps and consequently, the
 458 different DNIs, sun positions and heliostat areas for AI-training. The whole set was generated without
 459 supervision, as the digital twin iterated throughout the 931 conditions and the 17 heliostat combinations.
 460 It has been published [48] to enable deep-learning training tasks within CST applications. The images
 461 are stored in grayscale and in “.png” format to decrease the size of the dataset. It contains a
 462 “README.txt” file with the required instructions for further utilization as well as several illustrations
 463 of the virtual environment where the fluxes were simulated (reproducing the STJ).

464
 465 *4.3. U-Net based flux correction (sim2sim)*
 466

467 In this section, the authors present the U-Net sim2sim results. Here, the neural network's ability to
 468 self-correct the effect of the tracking error mathematical model under semi-controlled changing
 469 conditions is showcased. With this aim, the neural network has been trained by using the dataset from
 470 section 4.2. After a sensitivity analysis of accuracies, MSE losses and different hyperparameters, the
 471 authors found out the optimal configuration, detailed in Table 3 below. This training time has been
 472 achieved employing a single Nvidia A100 GPU.

473
 474 **Table 3.** Hyperparameters, and neural network training details.

Parameters	Values
Initial learning rate (-)	0.001
Learning rate scheduler	ReduceLROnPlateau
Learning rate reduction factor (-)	0.03
Total dataset size (-)	15928
Training size (%)	80
Batch size (-)	16
Loss function	L2-loss
Optimizer	AdamW
Epochs (-)	40
Final training loss (-)	0.0022
Final training accuracy (%)	98.7%
Training time (h)	10.3

475
 476
 477
 478
 479
 480
 481
 482
 483
 484
 485
 486
 487
 488 In order to assess these predictions, the authors analyse the peak deviation values, the MSE and a
 489 domain-specific accuracy metric. This function, introduced in eq. (11), studies the difference of total
 490 power between the prediction and the groundtruth.

$$A_{pix, X} = \frac{\sum_i |X_{r,i} - \hat{X}_{r,i}|}{\sum_i |\hat{X}_{r,i}|} \quad (11)$$

492 In this metric, $X_{r,i}$ represents the normalized 1-channel (grayscale) input's flux value of pixel "i",
 493 and $\hat{X}_{r,i}$ represents the equivalent value for the groundtruth. Therefore, the sum of all of these pixels'
 494 values represent the normalized total groundtruth power (denominator). Meanwhile, the numerator
 495 shows the normalized power difference between input and groundtruth. Thus, the accuracy compares
 496 how deviated the predicted power is from the groundtruth.

497 In order to assess the neural network's self-correction ability, the authors tested the replication of
 498 the tracking error effects for a set of sixty-three combinations of sun positions, DNIs and focused
 499 heliostats. These boundary conditions differ from the events comprehended within the training dataset,
 500 with the aim of thoroughly testing U-Net's inference capabilities. DNIs between 100 W/m² and 900
 501 W/m² (every 100 W/m²) have been analysed for 7 different timesteps that aim to cover the most
 502 representative sun positions. The selected dates are 22-03, 21-06, and 01.08. Three timesteps are
 503 reproduced (09:00, 13:00 and 18:00 GMT+2) for the first two cases while only 15:00 is chosen for the
 504 third date. Together, these conditions cover elevations between 7° and 63° and azimuths between 90°
 505 and 270°. The accuracy and MSE results for these cases are summarized in Fig. 13.

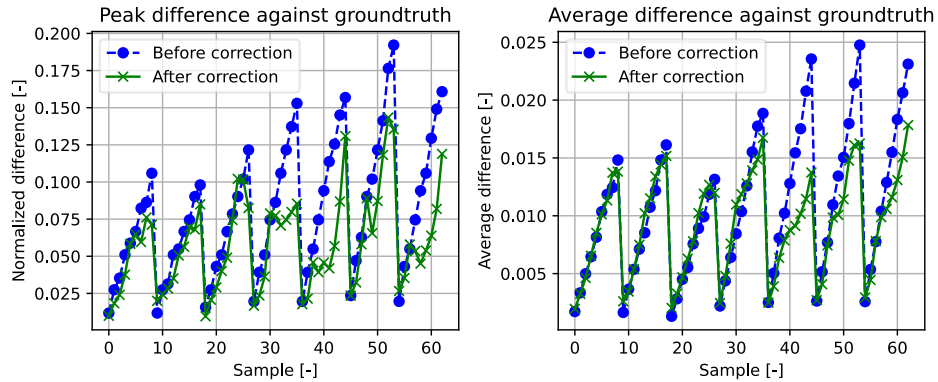
506 **Fig. 13.** Accuracy and MSE boxplots diagrams against DNI (above) and date (below) for the 63 samples. In the
 507 figure above, all of the 7 dates are grouped in a single boxplot diagram for the 9 different DNIs. In the figure
 508 below, all of the 9 DNIs are grouped in a single boxplot diagram for each of the dates.

509

510 The first row of the figure above depicts boxplots of accuracy and MSE against the DNI values.
 511 Each of the represented DNI values is simulated for each of the 7 timestamps mentioned before. All the
 512 average accuracies (represented by the orange lines) range from 86% at 100 W/m² to 91% at 900 W/m².
 513 The neural network shows robust behaviour for all the intermediate DNIs with accuracies around 90%.
 514 Due to the under-representation of DNIs between 200 W/m² and 400 W/m² in the dataset, the accuracy
 515 dispersion is slightly higher in this range. MSE losses shows a linearly increasing behaviour that can be
 516 explained by the higher absolute flux values present at higher DNI.

517 It is possible to analyse the accuracy and losses against the date in the row below. Once again,
 518 accuracies cluster around 90%, but results are now more scattered for the various inputs. Near solar
 519 noon (22-03-22@13:00:00, 21-06-22@13:00:00 and 01-08-22@15:00:00), accuracy shows solid results
 520 between 90 and 92.5% with outliers that reach almost 95%. When both accuracy graphs are cross-
 521 checked, it is possible to observe that these outlying values are reached at higher DNIs, as these are the
 522 most natural DNIs during solar noon and they are more widely present in the reality-based training
 523 dataset. Morning and evening results show accuracies between 88% and 90%, what substantiates the
 524 tuned U-Net's stability. However, its performance drops for 22-03-22@18:00:00, where average
 525 accuracy is below 85%. This timestep is weighed down by the presence of an outlier of 75% accuracy,
 526 corresponding to the case of 100 W/m². Low DNI and elevation angle (sunset at 18:50 on 22-03) justify
 527 this behaviour. The neural network is mostly trained for real operation hours, where it shows an
 528 outstanding and solid performance, so the accurate generalization of synthetic edge cases has little
 529 practical impact.

530 Additionally, it is relevant to examine the peak pixel-wise and the average differences before and
 531 after corrections, as well as the effect of the neural network across the whole flux distribution. The
 532 summary of the differences for the 63 analysed samples is shown in Fig. 14.



533 **Fig. 14.** Comparison of peak (left) and average (right) absolute differences between U-Net's input and
 534 groundtruth (blue line) and between output and groundtruth (green line) for the 63 samples. .

535 In the graphs above, the samples are ordered by increasing DNI (100 W/m^2 to 900 W/m^2) for each
 536 of the 7 timestamps. As seen in both plots, the original differences scale directly with DNI (blue lines).
 537 In terms of peak performance, the neural network corrects the original differences by 35% on average,
 538 with outstanding behaviour (corrections up to 65%) at DNIs over 500 W/m^2 . The results are flux
 539 distributions with deviations below 7.5% of groundtruth peak values. Even though peak differences are
 540 still biased because the metric considers every single pixel, including the natural local artifacts in deep-
 541 learning predictions, the correction is significant.

542 Average deviations are reduced by 55% of the original value, though this graph (figure above, right)
 543 should only be qualitatively studied, since the average difference values are weighed down due to the
 544 large non-irradiated regions, where the correction does not act. Finally, the authors evaluate differences
 545 between U-Net-predicted flux maps and their corresponding groundtruths. In this case, the accurate
 546 reproduction of the light beams' direction, radial shape and centre position is assessed for the 63
 547 samples. In Fig. 15, it is possible to check the results for the 7 samples where DNI was set to 900 W/m^2 .
 548 The most significant breakthrough observed in this plot is the accurate reproduction of the superposed
 549 fluxes for a wide sun position spectrum. As observed in the lower row, the center position and its flux
 550 value are perfectly predicted, with negligible differences, while light spots' tilt angle and shape deviate
 551 by less than 7.5% of the peak flux – what evidences the performance for the period of higher solar
 552 activity. The U-Net predictions only present some minor deformations in the contour compared to the
 553 groundtruths, and the same tilt angles.

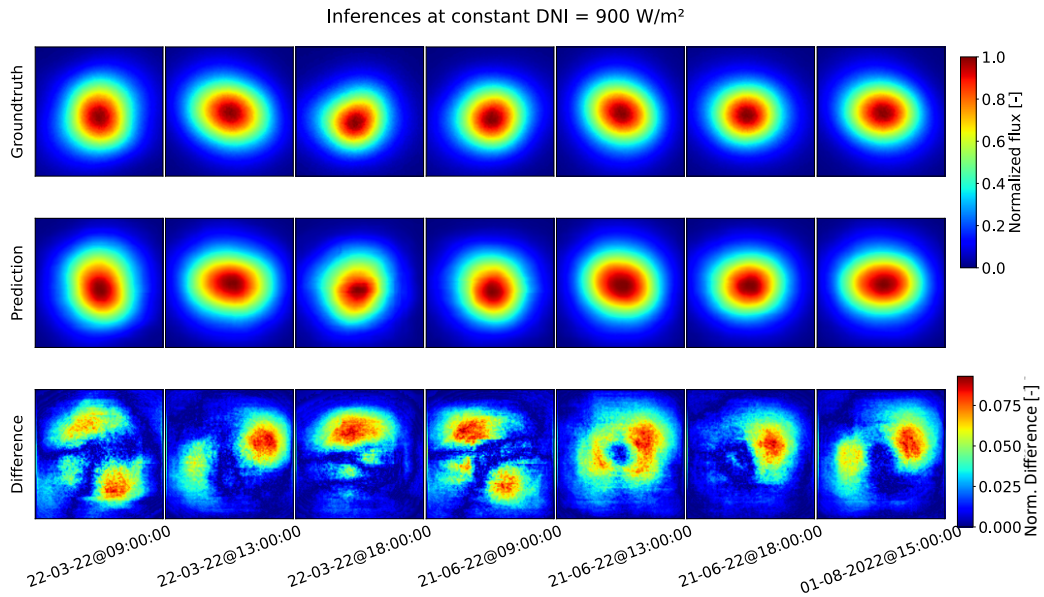


Fig. 15. Flux predictions (2nd row) against its corresponding groundtruth (1st row) for the seven timestamps with a DNI of 900 W/m². Normalized difference between each pair plotted in 3rd row.

556

557 5. Conclusion and outlook

558

559 The results presented above substantiate the main contributions of this methodology. This “ad-hoc”
 560 digital twin can be considered an innovative autonomous enabler for flux density and operation
 561 supervisions in near-real-time, thanks to the usage of a virtual environment. Low latencies (under 30
 562 seconds) can be expected when the data is live-tracked, as seen in result 4.1, which allows to detect
 563 malfunctions, as well as to optimize fluxes. They also demonstrate the capacity of the real-time data-
 564 agent hereby presented. Furthermore, the autonomy of this approach is substantiated by the creation of
 565 a training dataset that comprehends flux maps under 931 different meteorological conditions and 17
 566 different heliostat combinations, generated without human interaction (result 4.2). This finding means
 567 that synthetic datasets can be easily tailored for industrial power plants’ sim2sim superposed training,
 568 boosting the industrial relevance of this work.

569 Finally, the authors also present the findings related to a U-Net based self-correction, which
 570 addresses the need to get rid of mathematical models in accurate predictions. It has been successfully
 571 demonstrated that it is feasible to avoid tracking error models thanks to the usage of a trained neural
 572 network – evidenced by up to 93-95% of accuracy and peak differences below 7.5%. This result
 573 motivates the idea of also shedding the remaining mathematical models (CSR and atmospheric
 574 extinction), keeping the prediction accuracy. With this aim, the sim2real experimental campaign is being
 575 conducted nowadays (March 2025 to October 2025).

576 In addition, the novel training methodology based on superposed fluxes has been collaterally proven
 577 successful, what also raises industrial interest due to its relative simplicity. Whereas SOTA models are
 578 trained with individual heliostats, with sensitive training routines, it has been demonstrated that it is
 579 possible to develop an accurate prediction tool based on superposed fluxes. These high fluxes soften the
 580 individual importance of surface or tracking errors. This kind of training reduces the training time from
 581 57 h achieved by Lewen et al. to roughly 10 h. U-Net real-time corrections coupled with the DT pave
 582 the way to an AI-based industrial solution. To sum up, The model presented here does not only
 583 outperforms SOTA prediction results ([43] and [49] reached a 90%-92% of accuracy), but it also pushes
 584 industrial applications..

585 However, it is important to acknowledge the limits of this approach. For the moment, it is only
 586 possible to apply this method for one aimpoint and flat surfaces, due to parametric complexity.

587 Furthermore, deflectometric measurements are required prior to training, as well as periodical
588 calibrations when the plant characteristics vary.

589 Overall, the successful deployment of this tool represents a significant step towards fully
590 autonomous CSP plants. This powerful predicting model can replace the usage of conventional cameras
591 and boost the accuracy of FDM accuracy and applicability. The future work directly addresses multi-
592 aimpoint generalization, and adaptation to arbitrary receiver geometries. An extended training routine
593 is required to tackle the first of those challenges. The neural network needs to identify the functional
594 dependency between a stochastic set of aimpoints and the predicted flux map. Therefore, all the
595 meteorological conditions and sun positions will be replicated for a sufficiently varied set of aimpoint
596 combinations at the receiver aperture plane. For the latter challenge, a ray-level correction and projection
597 tool is being developed: each of the simulated rays is corrected by neural networks in power and
598 direction terms and then projected onto arbitrary surfaces (in “.stl” format). With these two advances, a
599 universal industrially-scaled flux density prediction tool will be developed and readily applicable.

600 CRediT authorship contribution statement

601 **Sergio Díaz Alonso:** Writing – original draft, visualization & editing; methodology, investigation,
602 conceptualization, software; validation. **Christian Raeder:** Writing – review & editing. **Bernhard**
603 **Hoffschmidt:** Writing – review; resources.

604 Declaration of competing interest

605 The authors declare that they have no known competing financial interests or personal relationships that
606 could have appeared to influence the work reported in this paper.

607 Data availability

608 Software can be made available on request with individual study of the case. Semi-controlled conditions
609 dataset made available on Zenodo repository: [10.5281/zenodo.13941464](https://zenodo.org/record/13941464)

610 Acknowledgments

611 Authors acknowledge the funding of European Union for this project (Horizon MSCA doctoral network,
612 project number 101072537).

613 6. Bibliography

614 Uncategorized References

- 615 [1] (2018). *A European strategic long-term vision for a prosperous, modern, competitive and*
616 *climate neutral economy.*
- 617 [2] F. J. Collado and J. Guallar, "A review of optimized design layouts for solar power tower plants
618 with campo code," *Renewable and Sustainable Energy Reviews*, vol. 20, pp. 142-154, 2013, doi:
619 10.1016/j.rser.2012.11.076.
- 620 [3] S. Hasni and W. J. Platzer, "Case study on decarbonization strategies for LNG export terminals
621 using heat and power from CSP/PV hybrid plants," *Solar Energy Advances*, vol. 3, 2023, doi:
622 10.1016/j.seja.2023.100041.
- 623 [4] E. Assareh *et al.*, "Thermodynamic assessment of a cogeneration system with CSP Driven-
624 Brayton and Rankine cycles for electric power and hydrogen production in the framework of
625 the energy and water nexus," *Energy Nexus*, vol. 5, 2022, doi: 10.1016/j.nexus.2021.100031.
- 626 [5] J. Li, "Scaling up concentrating solar thermal technology in China," *Renewable and Sustainable*
627 *Energy Reviews*, vol. 13, no. 8, pp. 2051-2060, 2009, doi: 10.1016/j.rser.2009.01.019.
- 628 [6] REN21, "Renewables 2024 Global Status Report Collection," 2024.
- 629 [7] U. Desideri and P. E. Campana, "Analysis and comparison between a concentrating solar and a
630 photovoltaic power plant," *Applied Energy*, vol. 113, pp. 422-433, 2014, doi:
631 10.1016/j.apenergy.2013.07.046.

- 632 [8] S. L. L. C. Group, "Assessment of Parabolic Trough and Power Tower Solar Technology Cost and Performance Forecasts," 10.2003 2003.
633
- 634 [9] H. Sumayli *et al.*, "Integrated CSP-PV hybrid solar power plant for two cities in Saudi Arabia,"
635 *Case Studies in Thermal Engineering*, vol. 44, 2023, doi: 10.1016/j.csite.2023.102835.
- 636 [10] M. I. Alam, M. M. Nuhash, A. Zihad, T. H. Nakib, and M. M. Ehsan, "Conventional and Emerging
637 CSP Technologies and Design Modifications: Research Status and Recent Advancements,"
638 *International Journal of Thermofluids*, vol. 20, 2023, doi: 10.1016/j.ijft.2023.100406.
- 639 [11] D. Lasluisa, D. Salas, N. Mazet, and D. Aussel, "Multidimensional analysis for the techno-
640 economic study of the CSP plant," *Journal of Energy Storage*, vol. 86, 2024, doi:
641 10.1016/j.est.2024.110732.
- 642 [12] S. P. Singh, D. K. Gupta, Y. Pradeep, S. Sachin, and K. Abhijeet, "Influence of process parameters
643 on capital cost, the efficiency of CSP based solar power plants- A review," *Materials today:
644 Proceedings*, vol. 62, 1, pp. 123-130, 2022 2022, doi:
645 <https://doi.org/10.1016/j.matpr.2022.02.606>.
- 646 [13] R. Pérez-Álvarez, A. Acosta-Iborra, and D. Santana, "Thermal and mechanical stresses in
647 bayonet tubes of solar central receivers working with molten salt and liquid sodium," *Results
648 in Engineering*, vol. 5, p. 100073, 2020/03/01/ 2020, doi:
649 <https://doi.org/10.1016/j.rineng.2019.100073>.
- 650 [14] A. Sánchez-González, M. R. Rodríguez-Sánchez, and D. Santana, "Allowable solar flux densities
651 for molten-salt receivers: Input to the aiming strategy," *Results in Engineering*, vol. 5, p.
652 100074, 2020/03/01/ 2020, doi: <https://doi.org/10.1016/j.rineng.2019.100074>.
- 653 [15] M. Röger, P. Herrmann, S. Ulmer, M. Ebert, C. Prah, and F. Göhring, "Techniques to Measure
654 Solar Flux Density Distribution on Large-Scale Receivers," *Journal of Solar Energy Engineering*,
655 vol. 136, no. 3, 2014, doi: 10.1115/1.4027261.
- 656 [16] M. Offergeld, M. Röger, H. Stadler, P. Gorzalka, and B. Hoffschmidt, "Flux density
657 measurement for industrial-scale solar power towers using the reflection off the absorber,"
658 presented at the SOLARPACES 2018: International Conference on Concentrating Solar Power
659 and Chemical Energy Systems, 2019.
- 660 [17] A. Sánchez-González and D. Santana, "Solar flux distribution on central receivers: A projection
661 method from analytic function," *Renewable Energy*, vol. 74, pp. 576-587, 2015/02/01/ 2015,
662 doi: <https://doi.org/10.1016/j.renene.2014.08.016>.
- 663 [18] N. R. E. L. (NREL). "Concentrated Solar Power Projects." NREL. [https://solarpaces.nrel.gov/by-
664 technology/power-tower](https://solarpaces.nrel.gov/by-technology/power-tower) (accessed 08.04.2024, 2024).
- 665 [19] D. Acosta, J. Garcia, M. Sanjuan, L. Oberkirsch, and P. Schwarzbözl, "Flux-feedback as a fast
666 alternative to control groups of aiming points in molten salt power towers," *Solar Energy*, vol.
667 215, pp. 12-25, 2021, doi: 10.1016/j.solener.2020.12.028.
- 668 [20] B. Belhomme, R. Pitz-Paal, and P. Schwarzbözl, "Optimization of Heliostat Aim Point Selection
669 for Central Receiver Systems Based on the Ant Colony Optimization Metaheuristic," *Journal of
670 Solar Energy Engineering*, vol. 136, no. 1, 2014, doi: 10.1115/1.4024738.
- 671 [21] L. L. Vant Hull, "The Role of "Allowable Flux Density" in the Design and Operation of Molten-
672 Salt Solar Central Receivers," *Journal of Solar Energy Engineering*, vol. 124, 2, pp. 165-169, April
673 24, 2002 2002, doi: 10.1115/1.1464124.
- 674 [22] Q. Yu, Z. Wang, and E. Xu, "Analysis and improvement of solar flux distribution inside a cavity
675 receiver based on multi-focal points of heliostat field," *Applied Energy*, vol. 136, pp. 417-430,
676 2014, doi: 10.1016/j.apenergy.2014.09.008.
- 677 [23] R. Osuna, R. Morillo, J. M. Jiménez, and V. Fernández-Quero, "Control and Operation Strategies
678 in PS10 Solar Plant," in *13th SolarPACES*, Sevilla, Spain, Jun. 20-23 2006, pp. 1-5.
- 679 [24] J. E. Pacheco, R. M. Houser, and A. Neumann, "Concepts to measure flux and temperature for
680 external central receivers," presented at the Joint Solar Engineering Conference, 1993-12-01,
681 1994.

- 682 [25] J. Ballestrín and R. Monterreal, "Hybrid heat flux measurement system for solar central
683 receiver evaluation," *Energy*, vol. 29, no. 5-6, pp. 915-924, 2004, doi: 10.1016/s0360-
684 5442(03)00196-8.
- 685 [26] O. Yogev, P. Gleckman, and M. Rozler, "High-Heat Solar Flux Scanner," in *SolarPACES 2009*,
686 Berlin, Germany, Sept. 15-18 2009.
- 687 [27] M. M. Elsayed, K. A. Fathalah, and O. M. Al-Rabghi, "MEASUREMENTS OF SOLAR FLUX DENSITY
688 DISTRIBUTION ON A PLANE RECEIVER DUE TO A FLAT HELIOSTAT," *Solar Energy*, vol. 54, 6, pp.
689 403-411, 1995, doi: 0038-092X(95)00010-0.
- 690 [28] G. von Tobel, C. Schelders, and M. Real, "Concentrated solar-flux measurements at the IEA-
691 SSPS solar-central-receiver power plant, Tabernas - Almeria (Spain). Final report. Technical
692 report No. 2/82," 1982.
- 693 [29] S. Ulmer, E. Lüpfert, M. Pfänder, and R. Buck, "Calibration corrections of solar tower flux
694 density measurements," *Energy*, vol. 29, no. 5-6, pp. 925-933, 2004, doi: 10.1016/s0360-
695 5442(03)00197-x.
- 696 [30] M. Thelen, C. Raeder, C. Willsch, and G. Dibowski, "A high-resolution optical measurement
697 system for rapid acquisition of radiation flux density maps.," in *SolarPACES 2016*, Abu Dhabi,
698 UAE, 2016, vol. 1850, no. 12: AIP Publishing, 2017, doi: 10.1063/1.4984534.
- 699 [31] C. K. Ho and S. S. Khalsa, "A Photographic Flux Mapping Method for Concentrating Solar
700 Collectors and Receivers," *Journal of Solar Energy Engineering*, vol. 134, no. 4, 2012, doi:
701 10.1115/1.4006892.
- 702 [32] B. Belhomme, R. Pitz-Paal, P. Schwarzbözl, and S. Ulmer, "A new fast ray tracing tool for high-
703 precision simulation of heliostat fields," *Journal of Solar Energy Engineering*, vol. 131, 2009,
704 doi: 10.1115/1.3139139.
- 705 [33] M. J. Blanco, A. Mutuberría, P. Garcia, R. Gastesi, and V. Martin, "PRELIMINARY VALIDATION
706 OF TONATIUH," presented at the SolarPACES 2009 International Conference, Berlin, Germany,
707 2009.
- 708 [34] NREL, "SolTRACE: A New Optical Modeling Tool for Concentrating Solar Optics.," presented at
709 the ISEC 2003: International Solar Energy Conference, Kohala Coast, Hawaii, 2003.
- 710 [35] A. Rasheed, O. San, and T. Kvamsdal, "Digital Twin: Values, Challenges and Enablers From a
711 Modeling Perspective," *IEEE Access*, vol. 8, pp. 21980-22012, 2019.
- 712 [36] B. Xu *et al.*, "A case study of digital-twin-modelling analysis on power-plant-performance
713 optimizations," *Clean Energy*, vol. 3, no. 3, pp. 227-234, 2019, doi: 10.1093/ce/zkz025.
- 714 [37] J. Yu, P. Liu, and Z. Li, "Hybrid modelling and digital twin development of a steam turbine
715 control stage for online performance monitoring," *Renewable and Sustainable Energy Reviews*,
716 vol. 133, 2020.
- 717 [38] O. Oñederra, F. J. Asensio, P. Eguía, E. Perea, A. Pujana, and L. Martinez, "MV Cable Modeling
718 for Application in the Digital Twin of a Windfarm," *2019 International Conference on Clean
719 Electrical Power (ICCEP)*, pp. 617-622, 2019.
- 720 [39] D. Ortiz Machado *et al.*, "Digital twin of an absorption chiller for solar cooling," *Renewable
721 Energy*, vol. 208, pp. 36-51, 2023, doi: <https://doi.org/10.1016/j.renene.2023.03.048>.
- 722 [40] D. O. Machado *et al.*, "Digital twin of an absorption chiller for solar cooling," *Renewable
723 Energy*, 2023.
- 724 [41] M. Pargmann, "A Digital Twin Environment for In-Situ Solar Tower Plant Optimization," RWTH
725 Aachen, 2023.
- 726 [42] M. Pargmann, J. Ebert, D. Maldonado Quinto, R. Pitz-Paal, and S. Kesselheim, "In-Situ Solar
727 Tower Power Plant Optimization by Differentiable Raytracing," *Nature Communications*, 2023.
- 728 [43] M. Kuhl, M. Pargmann, M. Cherti, J. Jitsev, D. M. Quinto, and R. Pitz-Paal, "In-Situ UNet-Based
729 Heliostat Beam Characterization Method for Precise Flux Calculation Using the Camera-Target
730 Method," ed: Research Square, 2024.
- 731 [44] J. Lewen, M. Pargmann, M. Cherti, J. Jitsev, R. Pitz-Paal, and D. M. Quinto, "Scalable heliostat
732 surface predictions from focal spots: Sim-to-Real transfer of inverse Deep Learning

733 Raytracing," *Solar Energy*, vol. 300, p. 113726, 2025/11/01/ 2025, doi:
734 <https://doi.org/10.1016/j.solener.2025.113726>.

735 [45] I. Miadowicz, D. M. Quinto, R. Pitz-Paal, and M. Felderer, "An action research study on the
736 digital transformation of concentrated solar thermal plants," *Solar Energy Advances*, vol. 5, p.
737 100102, 2025/01/01/ 2025, doi: <https://doi.org/10.1016/j.seja.2025.100102>.

738 [46] O. Ronneberger, P. Fischer, and T. Brox, "U-Net: Convolutional Networks for Biomedical Image
739 Segmentation," *ArXiv*, vol. abs/1505.04597, 2015.

740 [47] Y. Liu, L. Ji, R. Huang, T. Ming, C. Gao, and J. Zhang, "An attention-gated convolutional neural
741 network for sentence classification," *Intelligent Data Analysis*, vol. 23, no. 5, pp. 1091-1107,
742 2019, doi: 10.3233/ida-184311.

743 [48] S. Diaz Alonso and C. Raeder. *Concentrating solar power (CSP) plants AI-training dataset for
744 flux density measurements.*, doi: 10.5281/zenodo.13941464.

745 [49] J. Lewen, M. Pargmann, M. Cherti, J. Jitsev, R. Pitz-Paal, and D. M. Quinto, "Inverse Deep
746 Learning Raytracing for heliostat surface prediction," *Solar Energy*, vol. 289, p. 113312,
747 2025/03/15/ 2025, doi: <https://doi.org/10.1016/j.solener.2025.113312>.

748
749
750